Experimental Measurement of the Boundary Layer Velocity Field Induced by Water Waves Propagating Over a Ripple Bed

Phillip L.-F. Liu
Edwin A. Cowen
Khaled A. Al-Banaa
School of Civil & Environmental Engineering
Hollister Hall, Cornell University
Ithaca NY 14853-3501

ABSTRACT

The surface-wave induced boundary-layer flow field over a fixed ripple bed was studied using particle tracking velocimetry. The surface wave phase-dependent mean velocity and vorticity fields are presented for one-half wave period (the system is essentially, although not exactly symmetric) showing the vorticity generation and ejection process. The wave-induced streaming (mass flux) profile is determined and its implications discussed. The Reynolds stress, turbulence production, and turbulent kinetic energy at a single phase are presented and discussed.

INTRODUCTION

Sand ripples are frequently found on the seafloor. The appearance of sand ripples affects the sediment transport rate and causes additional energy dissipation. The flow motions, including oscillatory and steady components, directly influence the formation and stability of sand ripples. In recent years, many researchers have investigated analytically the relationships between boundary layer flow patterns and various physical parameters, such as the ripple slope, Reynolds number and Keulegan-Carpenter number (e.g., Longuet-Higgins, 1981; Vittori, 1989; Hara and Mei, 1990; Blondeaux and Vittori, 1991; Vittori and Blondeaux, 1996). Although these investigations have provided significant physical insights, they are limited to two-dimensional laminar flows. When turbulent conditions are allowed, the problem has proved intractable to analytic techniques and only numerical solutions have been obtained (e.g., Sato, *et al.*, 1986; Tsujimoto, *et al.*, 1991). The development of appropriate turbulence closure model for oscillatory boundary layer flows is still a challenging research topic. To accomplish this task, accurate experimental data are essential.

All the reported velocity measurements above ripple beds have been obtained by single point measurement techniques; either by a hot-film velocimetry (e.g., Sawamoto, *et al.*, 1982) or laser-Doppler velocimetry (e.g., DuToit and Sleath, 1981; Sato *et al.*, 1987; Ranasoma and Sleath, 1992; Horikawa and Ikeda, 1990; Horikawa and Mizutani, 1992). Due to the nature of point measurement techniques, the spatial resolution of the reported data is low. Consequently, this data can not provide accurate information on the vorticity field and other physical variables associated with the turbulence field, such as the Reynolds stress and eddy viscosity. Recently, particle image velocimetry (PIV), a whole-field measurement technique, has been successfully employed in measuring the vorticity field in the vicinity of an object subject to either a steady current or an oscillatory flow (e.g., Lin and Rockwell, 1994; Lin and Rockwell, 1995; Eamshaw and Greated, 1998).

In this paper, we report an experimental study of the flow field above a fixed ripple bed, using digital particle tracking velocimetry (DPTV) as outlined in Cowen and Monismith (1997). This technique uses cross-correlation based PIV as an estimate of the velocity field allowing individual particles to be tracked accurately at traditional PIV seeding densities. The result is an order of magnitude more independent velocity vectors as well as improved accuracy relative to traditional correlation based PIV. This allows us to investigate the generation and transport of vorticity and turbulence under various wave conditions.

EXPERIMENTAL SET-UP

The experiments were conducted in the wave tank in the DeFrees Hydraulics Laboratory at Cornell University. The wave tank is 32m long, 0.6m wide and 0.9m deep. It is constructed of plate glass sidewalls with a painted steel bottom. The middle test section has been fitted with a two-

dimensional rippled bed constructed of painted wood with the mean position between the ripple crest and trough aligned vertically with the steel bottom. The ripple crests are perpendicular to the tank centerline. The ripple bed is 1.80 m long and consists of 60 periodic ripples, each 1.2 cm in height and 3.0 cm in length. The wave tank is equipped with a piston-type wave generator, which is driven by a hydraulic servo-system and is capable of generating both regular and irregular waves. The downstream section of the tank is fitted with a 1:20 sloping beach and horsehair (a packing material) to minimize the reflected wave energy. The

Table 1 Physical and dimensionless parameters

Quantity (symbol)	Value
Water depth (h)	0.200 m
Wave period (T)	2.10 sec
Wavelength (λ)	2.85 m
Wave height (H)	0.0244 m
Horizontal particle displacement (A)	0.030 m
Ripple amplitude (a)	0.006 m
Ripple wavelength (L)	0.030 m
Ripple slope (ε = a/L)	0.2
Wavelength ratio (b = L/ λ)	0.011
Keulegan-Carpenter no. (α = A/L)	1.0
Boundary layer thickness ($\beta^{-1} = [2\nu/\omega]^{1/2}$)	0.8 mm
Reynolds no. ($Re = \omega A^2/\nu$)	2700

reflection coefficient was measured at less than 5%. Table 1 lists the wave and associated dimensionless parameters of the experiment.

Images were collected with a Silicon Mountain Designs 1M60 digital CCD camera (1024 x 1024 pixel, 12-bit, 30 Hz). For the measurements reported herein the camera was fitted with a 45mm extension tube and a Nikkor 105mm f/2.5 lens. The PTV illumination source was a Spectra-Physics PIV-200 twin-pulsed Nd:YAG laser system (140 mJ/pulse, 10 Hz on each laser head). The light sheet was formed by a cylindrical lens (f = -50mm) and a spherical lens (f = 1.0m). This arrangement yielded an approximately 1 mm thick light sheet which was centered on the middle ripple trough (between ripple number 30 and 31) and located 13cm off of the tank centerline. The camera image area was centered in this light sheet and the optical arrangement yielded a viewing area of 4.04cm x 4.04cm.

The camera-laser-wavemaker system was controlled with National Instruments Labview. A burst of 21 image pairs was collected at 10Hz directly to host computer RAM, evenly sampling the 2.1 second wave period. The time between the images in a pair was 4 ms. This process was repeated, approximately once per minute, 333 times. The DPTV algorithm tracked 7.7 million valid velocity vectors across all of the 21 phases. These vectors were ensemble averaged at the 21 phases into non-overlapping 1.26 mm x 0.99mm bins across the 333 waves at approximately 1027 active measurement locations (there were at total of 1308 measurement sites, however approximately 281 were located beneath the ripple bed). An average of 358 vectors were included in the ensemble average in each bin. Notably near the boundaries the vector count in the bins drops but remains greater than 200 vectors per bin in essentially all bins except those bins adjacent to the boundaries.

The flow field was allowed to establish for 2 hours before measurements were initiated and the flow field was assumed to be at steady state. The minimum spin-up time was determined by monitoring the phase shift between the wavemaker driving signal and the water surface elevation measured at the test location with a resistance type wave gauge. After two hours the phase shift was constant.

EXPERIMENTAL RESULTS AND DISCUSSIONS

In this section, the experimental data for the phase-averaged velocity, vorticity, turbulent intensity, and Reynolds stress will be presented. In figure 1 the time history of the free surface displacement above the measurement area is shown. The circles and the associated number represent the phases at which experimental results are presented.

Phase-Averaged velocity

The spatial variations of the phase-averaged velocity field at different phases are shown in Figures 2 - 6. At the phase $\omega t = 1.74\pi$ (Figure 2), the wave field above the ripple bed is accelerating as the wave crest is approaching the measurement point. The velocity field above the ripple crests appears to be uniform in both vertical and horizontal directions. However, close to the ripple bed the velocity profiles in the vicinity of the ripple crest are very different from those near the ripple trough. Above the crest, the velocity increases first as the ripple bed is approached so as to satisfy the continuity and it vanishes on the boundary. On the other hand, in the neighborhood of ripple trough, the velocity decreases monotonically as the ripple bed is approached. Consequently, the fluid decelerates on the lee side (down slope) of the ripple crest and a reverse pressure gradient also exists. These features suggest the possibility of flow separation, which indeed occurs and is shown in the next phase ($\omega t = 1.93\pi$, Figure 3). It is interesting to point out that the flow separation occurs before the wave crest reaches the measurement point. Because of the flow separation, a lee vortex is developed and is convected towards the ripple trough. As the wave crest passes the measurement point, the ambient velocity above the ripple bed starts to decrease and the lee vortex continues its forward movement. However, at $\omega t = 0.30\pi$ (Figure 4), although the wave field is still moving forward (in the positive x-direction), the vortex has started to move backwards. As the ambient velocity decelerates further, the vortex begins to rise from the ripple crest where the vortex was originally generated (Figure 5). As the wave trough approaches the measurement point, the magnitude of the negative (backward) velocity near the ripple bed grows stronger. At $\omega t = 0.79\pi$ flow separation has occurred (Figure 6). Thus the generation, convection, and dissipation

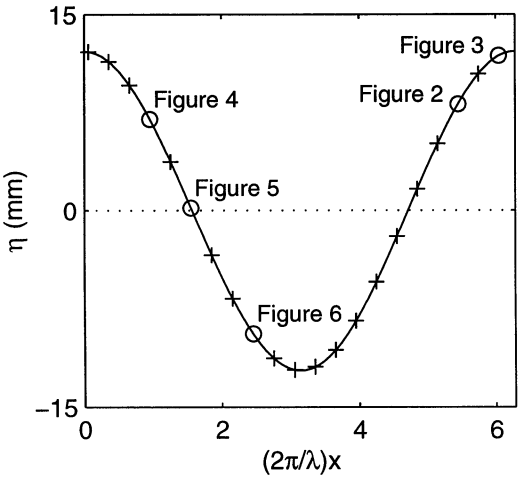

Figure 1. Surface wave phases measuremented.

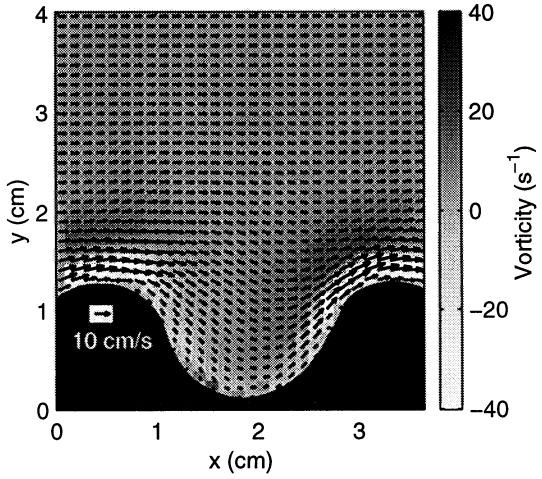

Figure 2. Velocity and vorticity field at $\omega t = 1.74\pi$

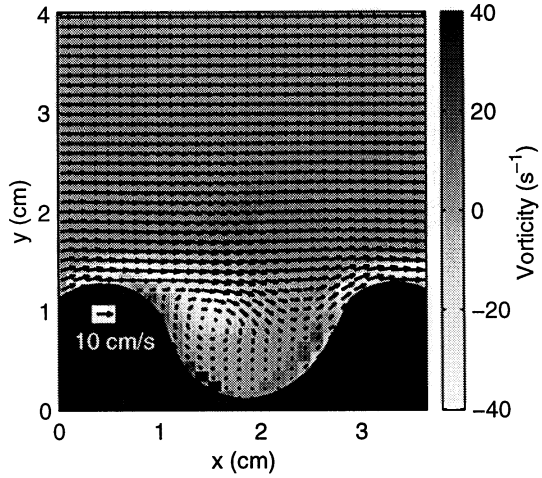

Figure 3. Velocity and vorticity field at $\omega t = 1.93\pi$

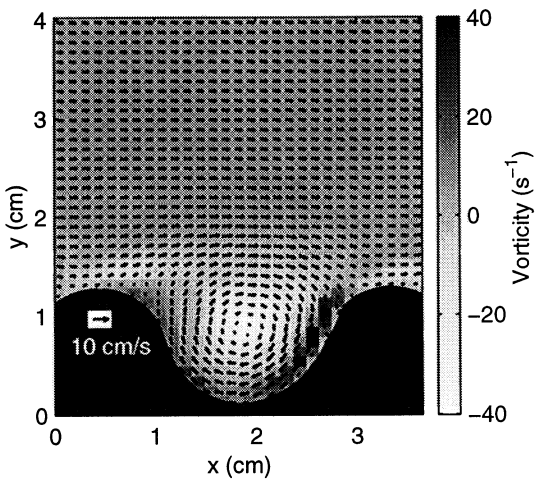

Figure 4. Velocity and vorticity field at $\omega t = 0.30\pi$

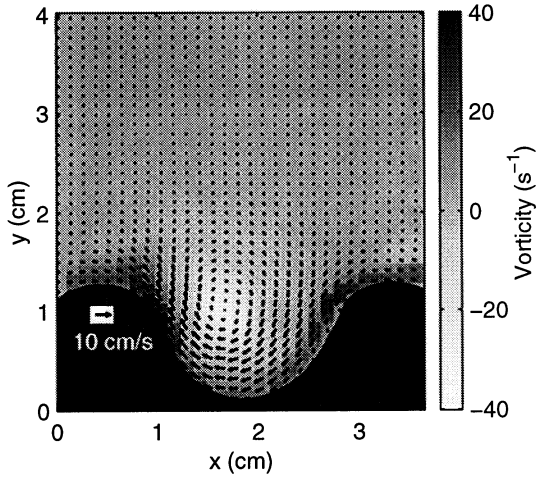

Figure 5. Velocity and vorticity field at $\omega t = 0.50\pi$

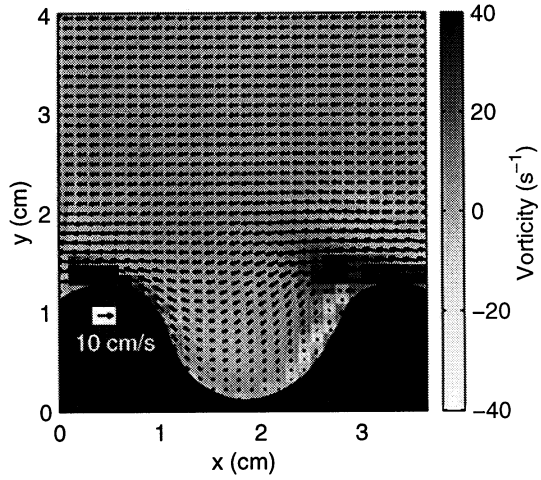

Figure 6. Velocity and vorticity field at $\omega t = 0.79\pi$

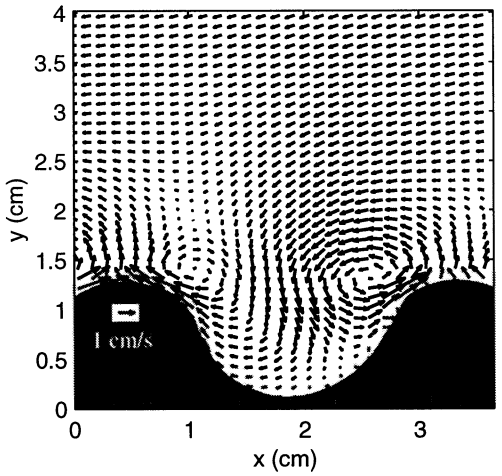

Figure 7. Mean wave-induced streaming field.

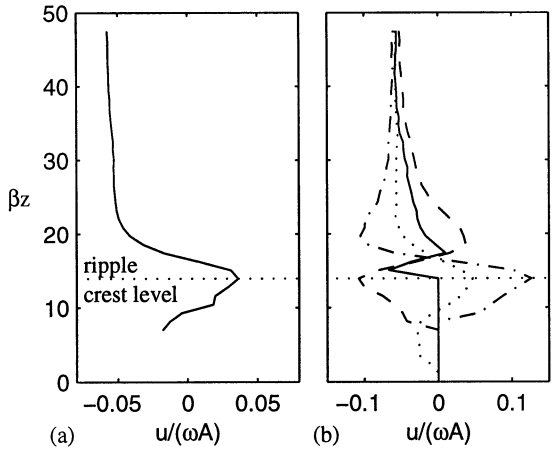

Figure 8. Mean wave-induced streaming profiles: (a) mean over entire wave period, (b) mean at four ripple positions: — ripple crest, --- minimum ripple slope, ··· ripple trough, – · maximum ripple slope.

of a vortex is repeated every half period. It is also noticed that the ejected vortex is transported across the ripple during the next half period for a distance of two and one-half of the ripple wavelengths. This can be seen more clearly when the vorticity field is examined.

Vorticity

One of the advantages of full-field imaging techniques like DPTV is the spatially resolved data enabling the calculation of the velocity gradients at each bin (a central difference was used) and hence the determination of the vorticity. It should be noted that since a central difference is used to determine the gradients the calculated vorticity in the bins immediately adjacent to the rippled bed should be used with caution. In Figures 2 - 6 the evolution of the vorticity over one-half wave period is displayed. The negative and positive vorticity corresponds to the clockwise and counterclockwise circulation, respectively. As the wave crest approaches the measurement point, strong negative vorticity is generated on the lee side of the ripple crest. A residual vortex with positive vorticity, which is generated and ejected from the previous wave period, remains on top of the newly generated vortex (Figure 6, it is apparent above the crests there is strong positive vorticity displacing weak residual negative vorticity). The pair of vortices is convected in the direction of wave propagation. The counterclockwise vortex moves faster than the clockwise vortex. The process repeats itself during the second half wave period with the opposite sense vorticity.

Wave-Induced Streaming

At some distance above the ripple bed the viscous forces become significant and not surprisingly the velocity field is affected. Clearly vorticity is generated at the ripple bed and is diffused upwards due to viscosity. This process is balanced by the Reynolds stress and the rectified result is a vertically dependent phase shift in the mean forcing. The phenomenon, known as wave-induced streaming, was first analytically explained by Longuet-Higgins (1953), although evidence of near-bed wave-induced mean currents were noted much earlier. Taking the mean of the 21 phase-averaged velocity fields (shown in Figure 1) yields the wave-period averaged wave-induced streaming field shown in Figure 7. Near the ripple bed two recirculating cells appear, which are not symmetric with respect to the ripple trough. The asymmetry is a result of the mean net-negative wave-induced drift current that is evident just outside the bottom boundary layer. This net-negative current has been seen by many researchers in laboratory wave facilities (e.g., Kemp and Simons, 1982; Nepf *et al.*, 1995; Swan, 1990). The negative mean drift is generally assumed to be the result of continuity in closed basins, however, Monismith *et al.* (1999) propose that it is the result of the wavemaker boundary condition and exactly cancels the Lagrangian wave-induced drift, resulting in zero net mass flux locally as a function of depth.

The magnitude and the direction of the steady streaming velocity have direct influence on the sediment transport and the stability of a ripple bed. The two recirculating cells clearly are a strong mechanism to transport sediment mass from the ripple trough to the ripple crest and hence likely contribute to ripple amplitude growth.

The ripple-length averaged (average from crest-to-crest in Figure 7) streaming velocity field is shown Figure 8a and is a measure of the streamwise component of the Eulerian mass flux. Four profiles of the streaming velocity (streamwise component) are shown in Figure 8b. It is clear that our measurement region encompassed the entire wave-induced boundary layer as the streaming velocity becomes essentially independent of both ripple phase and distance above the bed by about $\beta z = 25$. The boundary layer appears thicker than the standard laminar solution over a flat bed (see Longuet-Higgins, 1953) where the thickness is $\beta z \approx 3$. This is a result of the turbulence

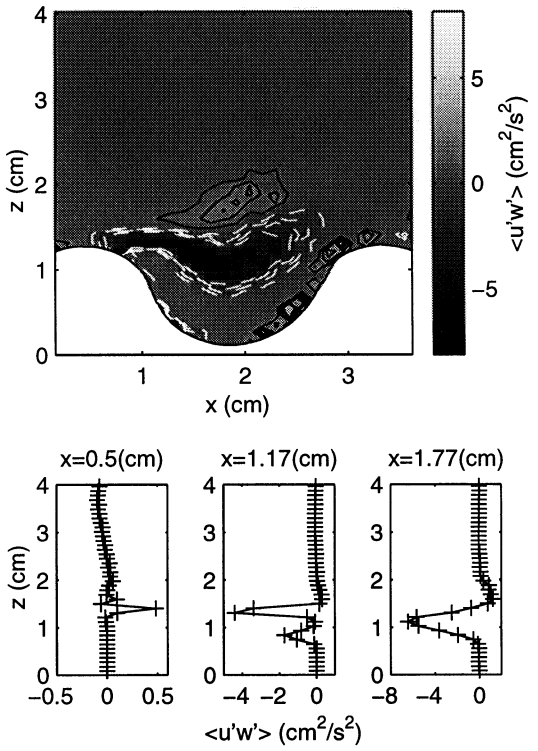

Figure 9. Reynolds stress field and profiles at $\omega t = 1.93\pi$

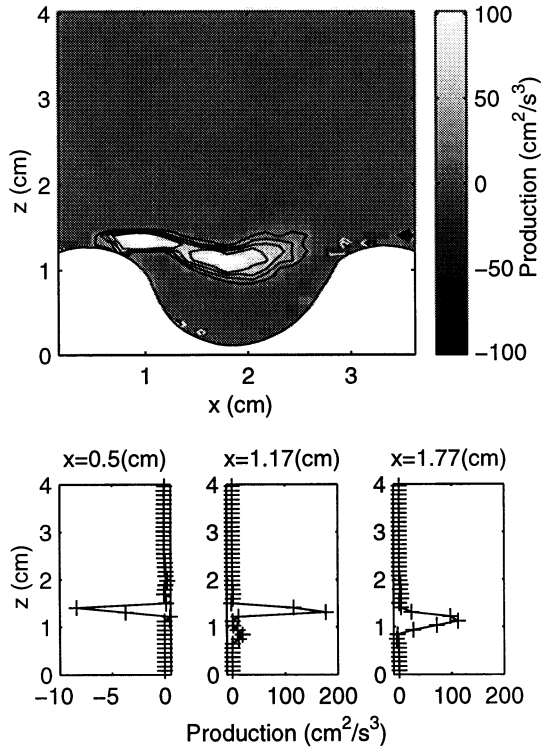

Figure 10. Turbulence production field at $\omega t = 1.93\pi$

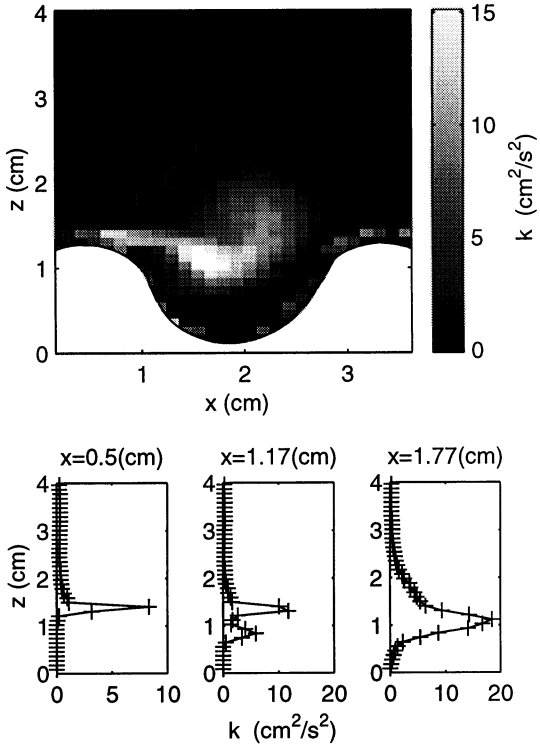

Figure 11. Turbulence intensity, k, at $\omega t = 1.93\pi$

enhancement by the ripple bed interacting with the wave-induced mean flow.

Reynolds Stress and Turbulence Production and Turbulence Intensity

An advantage of quantitative imaging techniques is the ability to calculate spatial gradient fields as well as the Reynolds stress and hence the turbulence shear production, defined as:

$$\wp = \langle u'w' \rangle \left(\frac{\partial u}{\partial z} + \frac{\partial w}{\partial x} \right) \tag{1}$$

Figure 9 shows the Reynolds Stress field at one surface wave phase. The strong ripple-bed phase dependent Reynolds stress clearly occurs in a region of high shear (Figure 3). Figure 10 shows the turbulence shear production at the phase corresponding to Figures 3 and 9. The Reynolds stress is seen to correlate strongly with the strong shear associated with the shear zone between the negative vorticity being newly generated at the bed and the residual positive vorticity from the previous half wave period that has diffused away from the bed (as seen in Figure 3). In fact the diffused residual positive Reynolds stress from the previous half-period shear zone is also present.

Two components of the turbulence kinetic energy, k, can be measured directly with the DPTV technique, u'^2 and w'^2.

We can conservatively estimate k by assuming that the turbulence is isotropic, hence

$$k = \frac{3}{4}\left(u'^2 + w'^2\right) \quad (2)$$

Figure 11 shows the turbulent kinetic energy at the same surface wave phase as the data shown in Figures 9 and 10. The spatial evolution of the turbulent patch is clear looking at the profiles. The turbulent kinetic energy is being produced near the crest and while production continues throughout the shear layer at the ripple crest level, diffusion is clearly evident looking at the growing width of the k spike in the three profiles shown.

CONCLUSIONS

DPTV has been demonstrated as a powerful tool for obtaining information on the temporal and spatial variation of many flow variables inside the surface wave-induced boundary layer above a fixed ripple bed. The generation, convection, and dissipation of vorticity between two adjacent ripple crests are clearly captured by DPTV. From the experimental data, the wave-induced streaming, Reynolds stress, turbulence production, and turbulent kinetic energy can also be calculated.

Using different wave and ripple parameters, additional experiments will be performed in the future so that the relationship between the vorticity and turbulence fields and related parameters can be examined. We are particularly interested in this flow physics as it relates to the growth and stability of ripples. This data set will be used to verify existing, and develop new models of ripple formation and sediment entrainment at a ripple bed.

ACKNOWLEDGMENTS

We gratefully acknowledge the financial support from the National Science Foundation (CTS-9808542, CMS-9528013) and the Office of Naval Research (N00014-98-1-0774), Program Officer: Dr. Keith Ward.

REFERENCES

Blondeaux, P., and Vittori, G., 1991, "Vorticity Dynamics in an Oscillatory Flow Over a Rippled Bed," *Journal of Fluid Mechanics*, Vol. 226, pp. 257-289.

Cowen, E.A., and Monismith, S.G., 1997, "A hybrid digital particle tracking velocimetry technique," *Experiments in Fluids*, Vol. 22, pp. 199-211.

DuToit, C.G., and Sleath, J.F.A., 1981, "Velocity Measurements Close to Ripple Beds in Oscillatory Flow," *Journal of Fluid Mechanics,* Vol. 112, pp. 71-96.

Eamshaw, H.C., and Greated, C.A., 1998, "Dynamics of Ripple Bed Vortices," *Experiments in Fluids*, Vol. 25, pp. 265-275.

Kemp, P. and Simons, R., 1982, "The interaction between waves & a turbulent current: waves propagating with the current," *Journal of Fluid Mechanics*, Vol. 116, pp. 227-250.

Hara, T. and Mei, C.C., 1990, "Oscillating Flows Over Periodic Ripples," *Journal of Fluid Mechanics*, Vol. 211, pp. 183-209.

Horikawa, K. and Mizutani, S., 1992, "Oscillatory Flow Behavior in the Vicinity of Ripple Models," *Proceedings, 23rd International Conference on Coastal Engineering*, ASCE, pp. 212-2135.

Horikawa, K.,and Ikeda, S., 1990, "Characteristics of Oscillatory Flow Over Ripple Models," *Proceedings, 22nd International Conference on Coastal Engineering*, ASCE, pp. 661-674.

Lin, J.-C., and Rockwell, D., 1995, "Evolution of a Quasi-Steady Breaking Wave," *Journal of Fluid Mechanics*, Vol. 302, pp. 29-44.

Lin, J.-C., and Rockwell, D., 1994, "Instantaneous Structure of a Breaking Wave," *Physics of Fluids*, Vol. 6, pp. 2877-2879.

Longuet-Higgins, M.S., 1981, "Oscillating Flow Over Steep Sand Ripples," *Journal of Fluid Mechanics*, Vol. 107, pp. 1-35.

Longuet-Higgins, M.S., 1953, "Mass transport in water waves," *Philosophical Transactions. Series A. Mathematical and Physical Sciences*, Vol. 245, pp. 535-581.

Monismith, S.G., Cowen, E.A., Nepf, H.M., Magnaudet, J.; Thais, L., 1999, "Mean flows under surface gravity waves", Submitted to *Journal of Fluid Mechanics.*

Nepf, H.M., Cowen, E.A., Kimmel, S.J., Monismith, S.G., 1995, "Longitudinal vortices beneath breaking waves," *Journal of Geophysical Research (Oceans)* Vol. 100, pp. 16,211- 16,221.

Ranasoma, K.I.M., and Sleath, J.F.A., 1992, "Velocity Measurements Close to Ripple Beds," *Proceedings, 23rd International Conference on Coastal Engineering*, ASCE, pp. 2383-2396.

Sato, S., Shimosako, K., and Watanabe, A., 1987, "Measurements of Oscillatory Turbulent Boundary Layer Flow above Ripples with a Laser-Doppler Velocimeter," *Coastal Engineering in Japan*, Vol. 30, pp. 89-98.

Sato, S., Uhara, H., and Watanabe, A., 1986, "Numerical Simulation of the Oscillatory Boundary Layer Flow Over Ripples by a κ–ε Turbulence Model," *Coastal Engineering in Japan*, Vol. 29, pp. 65-78.

Sawamoto, M., Yamashita, T., and Kitamura, T., 1982, "Measurements of Turbulence Over Vortex Ripple," *Proceedings, 18th International Conference on Coastal Engineering*, ASCE, pp. 282-296.

Swan, C., 1990, "Convection within an experimental wave flume," Journal of Hydraulic Research, Vol. 28, pp. 273-282.

Tsujimoto, G., Hayakawa, N., Ichiyama, M., Fukushima, Y., and Nakamura, Y., 1991, "A Study on Suspended Sediment Concentration and Sediment Transport Mechanism Over Rippled Sand Bed Using a Turbulence Model," *Coastal Engineering in Japan*, Vol. 34, pp. 177-189.

Vittori, G. and Blondeaux, P., 1996, "Mass Transport Under Sea Waves Propagating Over a Rippled Bed," *Journal of Fluid Mechanics*, Vol. 314, pp. 247-265.

Vittori, G., 1989, "Nonlinear Viscous Oscillatory Flow Over a Small Amplitude Wavy Wall," *Journal of Hydraulic Research*, Vol. 27(2), pp. 267-280.